BALTICA ISSN: 0067-3064
2024 37(8)

Transformation Processes of Hydrogen Titanate Nanotubes into Diverse Titanium Dioxide Nanostructures for Advanced Photocatalysis and Antibacterial Applications

Nur Adibah Roslan[a], Asnuzilawati Asari[a], Mahani Yusoff[c], Runkang Cai[d], Mohd Hasmizam Razali[a,b*]
[a]Faculty of Science and Marine Environment, Universiti Malaysia Terengganu, 21030 Kuala Nerus, Terengganu, MALAYSIA
[b]Advanced Nanomaterials Research Group, Faculty of Science and Marine Environment, Universiti Malaysia Terengganu, 21030 Kuala Nerus, Terengganu, MALAYSIA
[c]Faculty of Bioengineering and Technology, Universiti Malaysia Kelantan Kampus Jeli,
17600 Jeli, Kelantan, MALAYSIA
[d]Department of Network Technology, Software Engineering Institute of Guangzhou, Guangdong Province, 510000, China
Correspondence: mdhasmizam@umt.edu.my

Nanostructured TiO_2 were synthesized by using the hydrothermal method. Their physiochemical properties were characterized using FTIR, FESEM, XRD, BET and tested as antibacterial materials as well as photocatalyst for MO degradation. FTIR analysis showed the presence of O-H and Ti-O bonds for all samples studied. The phase and morphological structures of nanostructured TiO2 is dependent on the calcination temperature. The FESEM and TEM results showed that TiO2 nanotubes and TiO2 nanoparticles produced from hydrogen titanate after calcination at temperatures of 400 and 700. While at a temperature of 500, there is mixing between TiO_2 nanotubes and nanoparticles. XRD analysis shows that as-synthesized is hydrogen trititanate while after calcination at temperatures of 400, 500 and 700 for 2 hours, TiO_2 anatase is formed. The TiO_2 nanotubes and nanoparticles exhibits large specific surface areas between 300 to 30 m^2/g, thus displays good photocatalytic activity and antibacterial properties. The TiO_2 nanotube structure has the best performance which successfully degrades 80% of methyl orange (MO) and a 15.44±0.26 mm inhibition zone against *S. aureus* was obtained at 0.20 M.

Keywords: *Nanomaterials; metal oxide; photocatalyst; antibacterial.*

1. Introduction

Titanium dioxide (TiO_2) naturally occurs in three crystalline polymorphs: anatase, brookite, and rutile, which are commonly encountered in various applications. The crystal phase plays a crucial role in determining the photocatalytic performance of TiO_2, with the formation of surface-phase junctions being identified as an effective strategy for enhancing photocatalytic efficiency [1-3]. For example, Degussa P25 TiO_2, comprising anatase and rutile, is frequently utilized as a benchmark model photocatalyst due to its high activity [4]. Numerous endeavors have focused on designing biphasic TiO_2 compositions, such as anatase and rutile, anatase and brookite, or brookite and rutile, as well as TiO_2 with three mixed phases, to develop active photocatalysts. However, most previously reported hetero-phase TiO_2 photocatalysts were either transformed from amorphous Ti-containing precursors or prepared via high-temperature calcination, resulting in low specific surface area [5].

Additionally, the systematic correlation between TiO_2 surface phase and catalytic performance remains poorly understood, particularly regarding TiO_2 compositions with mixed phases of anatase, brookite, and rutile, due to the lack of precise preparation methods for controlling the phase structure of TiO_2.

In recent times, hydrogen titanate (H-titanate) nanotubes and nanofibers have garnered significant interest due to their unique structural characteristics, which consist of the same TiO_6 octahedron unit as TiO_2 [6]. The transition from H-titanates to various TiO_2 nanostructures under relatively mild hydrothermal conditions, achieved through the in-situ rearrangement of the common structural unit, has emerged as a prevalent method. Chemically reactive H-titanate precursors, particularly under acidic conditions, undergo readily transformation into diverse TiO_2 crystalline forms by dehydrating and rearranging TiO_6 octahedra. The resulting TiO_2's phase composition and morphology have been found to rely on several factors, including the type of H-titanate precursors used, the acidity or alkalinity of the environment, and the hydrothermal conditions.

Notably, the soft chemical transformation can lead to the conversion of H-titanate into pure rutile TiO_2 crystalline in concentrated acid solutions (above 2.0 M) or into pure anatase TiO_2 in diluted acid (below 0.10 M) or even neutral solutions [7]. However, the transition from H-titanate to TiO_2 polymorphs in intermediate-concentration acid solutions between 0.10 and 2.0 M remains poorly explored, yielding diverse and inconclusive results. For instance, H-titanate nanotubes treated in a 0.10 M acidic solution have yielded TiO_2 with predominant anatase and minor rutile, comparable mixtures of anatase and rutile, or even pure rutile. Additionally, at a pH of 0.5, a combination of rutile and brookite or predominant rutile with minor anatase has been reported. Furthermore, transformations from ammonium-exchanged and potassium titanate to TiO_2 with varying shapes and phases have also been documented [8]. Given that H-titanate and TiO_2 share the same TiO_6 octahedron unit, the transition from H-titanate presents a novel approach for preparing TiO_2 samples featuring diverse surface-phase junctions. In this study, we conducted a systematic examination of the phase structure of TiO_2 samples obtained through controlled phase transition from H-titanate nanotube precursors under various calcination temperature alongside their antibacterial and photocatalytic activity.

2. Materials and methods

2.1 Sample preparation

2.0 gram of TiO_2 powder precursor (Merck) was dispersed in 10 M NaOH (100 ml) with constant stirring for 30 minutes (500 rpm). Then, the mixture was sonicated in sonicator bath for 30 minutes, after that continue with constant stirring for 30 minutes (500 rpm). Subsequently, the mixture was transferred into Teflon vessel and subjected to hydrothermal treatment at 150 °C for 24 hours in autoclave. When the reaction was completed, the white solid precipitate was collected and dispersed into 0.1 M HCL (200 ml) with continuous stirring for 30 minutes (500 rpm) for washing. Then, the washing was followed by distilled water until the pH of washing solution was 7 and subsequently dried at 80 °C for 24 hours in an oven to produce a powder denoted as HT150. Then, the obtained sample powder (HT150) was calcined at 400 °C, 500 °C, and 700 °C for 2 hours to produce the treated samples named as HT150/400, HT150/500, and HT150/700 samples, respectively.

2.2 Characterization

ATR-FTIR spectra were collected using a Perkin Elmer Spectrum 100 FT-IR spectrophotometer with a PIKE Miracle ATR accessory (single-bounce beam path, 45° incident angle, 16 scans, 4 cm^{-1} resolution). An advanced ATR correction was applied to all spectra in the region from 4000 to 600 cm^{-1}. XRD diffractogram was performed by using Rigaku Miniflex (II) X-ray diffractometer operating at a scanning rate of 2.00° min^{-1}. The diffraction spectra were recorded at the diffraction angle, 2θ from 10° to 80° at room temperature. Field Emission Scanning Electron Microscope (FESEM) micrograph was captured using ZEISS SUPRA^{TM} 35VP FESEM coupled with EDX for morphological and elemental analysis. The characterization was done by grinding the sample into fine powder before adhering them onto a flat surfaced of an aluminium sample stub that was stuck with a double-sided carbon tape. The doubled-sided carbon tape was used to ensure that the sample is able to withstand on the stub while scanning was done. The sample studied comprise of metal oxides which are non-conducting, thus may need to be coated with a conducting medium before FESEM investigation. The sample was placed in a Bio Rad SEM coating system apparatus to be coated with gold using a gold spulter at 10^{-1}Mbar. The purpose of the coating is to eliminate any possible discharged of powder sample. BET surface area analysis was studied by using Micromeritics ASAP2020 (Alaska) to determine the surface area and pores size distribution. The nitrogen adsorption and desorption was measured at 77 K (temperature of liquid nitrogen) and the samples were degassed in a vacuum at 110 °C under nitrogen flow for overnight prior to analysis.

2.3. Photocatalytic activity

The photocatalytic activity of the synthesized samples was assessed for the photodegradation of MB. For the photodegradation process, 10 mg of each catalyst powder was individually dispersed in 60 ml of dye aqueous solution at a specific concentration (5 ppm). Prior to the photocatalytic test, the mixed solution was magnetically stirred in the dark for 1 hour to achieve adsorption/desorption equilibrium between the dye and catalyst. A specific volume (5 ml) of the initial concentration (C_o) solution was then extracted and exposed to a 30 W LED lamp. Throughout the reaction process, the reactant mixtures were continuously stirred, and samples were extracted at regular intervals (60 minutes) to determine the degradation of the dye. The removed suspensions underwent centrifugation (6000 rpm for 10 minutes) for solid-liquid separation. The temporal variation in the concentration of MB dye was monitored by examining the change in absorption peaks using a UV–vis spectrometer (Perkin Elmer Lambda 35 UV-Vis). The photo-degradation efficiency (η) was calculated using Equation 1::

$$\text{Degradation } (\eta) = \frac{C_0 - C_t}{C_0} \times 100 \qquad \text{Equation 1}$$

Where C0 represents the initial absorption of MB and Ct represents the absorption of MB after the reaction at time t.

2.4 Antibacterial study

For the antibacterial study, Gram-positive bacteria (*Staphylococcus aureus*) were utilized in the antibacterial assay. The standard growth medium, Muller-Hinton (MH) agar (DifcoTM), was prepared and sterilized using an autoclave at 120°C for 15 minutes. Before bacterial inoculation, Staphylococcus aureus was sub cultured in MH agar and incubated aerobically at 37°C for 24 hours to ensure bacterial stability without contamination. Bacterial concentrations were determined by measuring optical density using a Spectrophotometer (Biomerieux Densicheck Plus) at 600 nm. In this investigation, bacterial suspensions were adjusted to equivalent turbidity based on 0.5 McFarland standards. Staphylococcus aureus inoculants were evenly distributed on sterile petri plates containing MH agar. Using a sterile cotton swab, all bacteria were spread evenly over the agar plate surface. Samples of optimum photocatalyst powder at the various concentration and penicillin as a control were gently applied to the agar. Penicillin served as the standard antibiotic for positive control. The plates with samples and agar containing bacteria were then incubated at 37°C for 24 hours in triplicates. Observations of clear zones on each plate were recorded after 24 hours of incubation at 37°C, indicating microbial growth inhibition

3. Results and discussion

Fig. 1 presents the Fourier Transform Infrared (FTIR) spectra of the HT150, HT150/400, HT150/500, and HT150/700 samples. The HT150 spectrum exhibits a broad peak in the 3700-2800 cm^{-1} range, characteristic of the OH stretching mode associated with surface hydroxyl groups. Additionally, the OH deformation mode observed in the 1800-1400 cm^{-1} range for all samples supports the presence of surface water molecules [9]. Notably, the HT150/400, HT150/500, and HT150/700 samples spectra show a significant decrease in the transmittance intensity of this peak, suggesting the elimination of water molecules from the sample surface. All studied samples (HT150, HT150/400, HT150/500, and HT150/700) display a broad peak below 650 cm^{-1} attributed to the Ti-O stretching vibrations of surface bridging oxides formed by the condensation of adjacent surface hydroxyl groups [10].

Fig. 2 depicts the X-ray diffraction (XRD) patterns of the samples. The HT150 sample exhibits peaks at $2\theta = 25.43°$ and 48.40°, consistent with hydrogen trititanate ($H_2Ti_3O_7$) as reported previously [11,12]. In contrast, the HT150/400, HT150/500, and HT150/700 samples exhibit peaks characteristic of anatase TiO_2, suggesting the transformation of hydrogen trititanate into this phase upon calcination at 400 °C and above. Anatase TiO_2 is identified by the presence of peaks at 25.4°, 37.9°, 48.2°, 54.1°, 55.15°, 62.74°, 70.37°, and 75.07°, with the most prominent peak around 25° [13]. This transformation likely occurs through a simple chemical reaction as depicted in Equation 1:

$$H_2Ti_3O_7 \rightarrow 3TiO_2 + H_2O \quad \text{(Eq. 1)}$$

These findings indicate the low thermal stability of hydrogen trititanate, as it decomposes to form anatase TiO_2 at relatively low calcination temperatures (starting from 400 °C). As the calcination temperature increases, the XRD peaks become sharper and narrower, signifying an enhancement in the crystallinity of the samples.

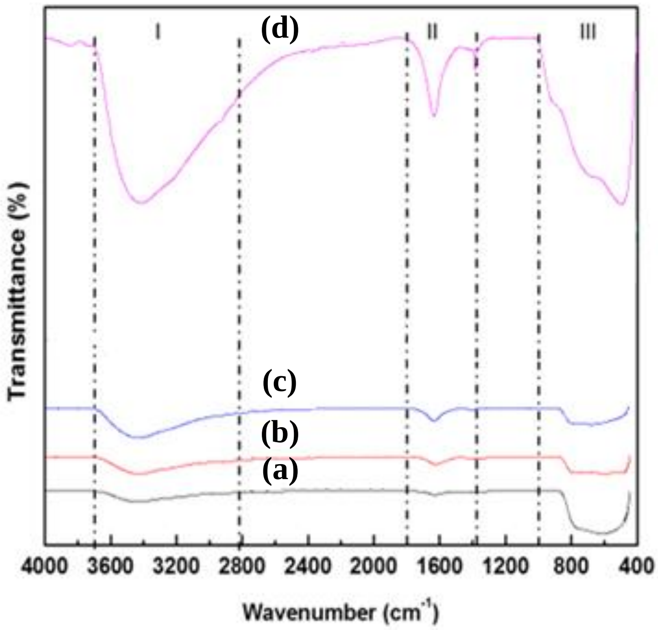

Figure 1: FTIR spectra of (a) HT150, (b) HT150/400, (c) HT150/500, and (d) HT150/700

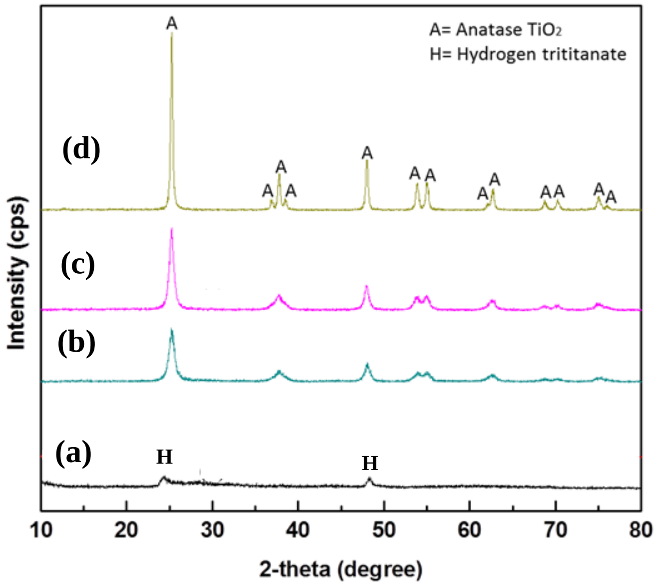

Figure 2: XRD diffractograms of (a) HT150, (b) HT150/400, (c) HT150/500, and (d) HT150/700

Fig. 3 illustrates FESEM micrographs depicting the morphology of the HT150, HT150/400, HT150/500, and HT150/700 samples. The HT150 sample exhibits a fibrous-like structure with diameters around 10 nm and lengths extending several hundred nanometers (Fig. 3(a). In the case of HT150/400, fibrous-like structures are visible, tending to aggregate (Fig. 3(b). However, for HT150/500, the isolated fibrous-like structures appear to have fragmented into smaller particles (Fig. 3(c). Upon closer examination by FESEM (inset in Fig. 3(c), the constituent particles of the fibrous structure become more discernible. HT150/700 displays agglomerated particles, evident in the micrographs due to the high calcination temperature of 700 °C (Fig. 4(d). Further morphology analysis was conducted using TEM, as depicted in Fig. 4. The TEM image of HT150 reveals the formation of nanotube products with diameters approximately 4 nm and 10 nm for inner and outer diameters, respectively (Fig. 4(a)). In the case of HT150/400, the nanotube structures retain their shape, albeit experiencing some aggregation due to heat treatment, resulting in a slight increase in the inner diameter of the nanotubes (Fig. 4(b). An et al. (2008) previously reported that treated nanotubes can maintain a tubular structure when calcined at 400 °C. Remarkably, for HT150/500, the material's morphology is significantly altered, with no observable nanotube structures; instead, small particles are produced (Fig. 4(c), indicative of nanotube destruction. A similar morphology is observed for HT150/700, where the presence of small particles is evident (Fig. 4(d)).

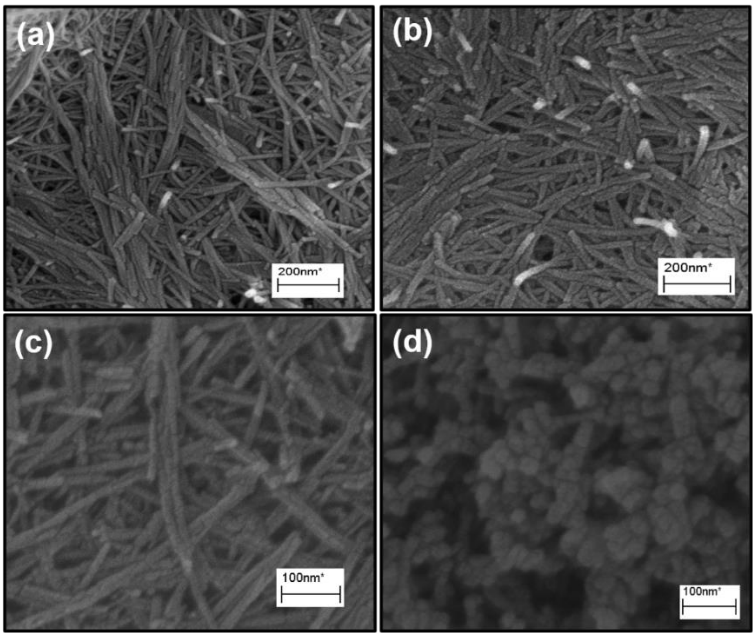

Figure 3: FESEM micrographs of (a) HT150, (b) HT150/400, (c) HT150/500, and (d) HT150/700

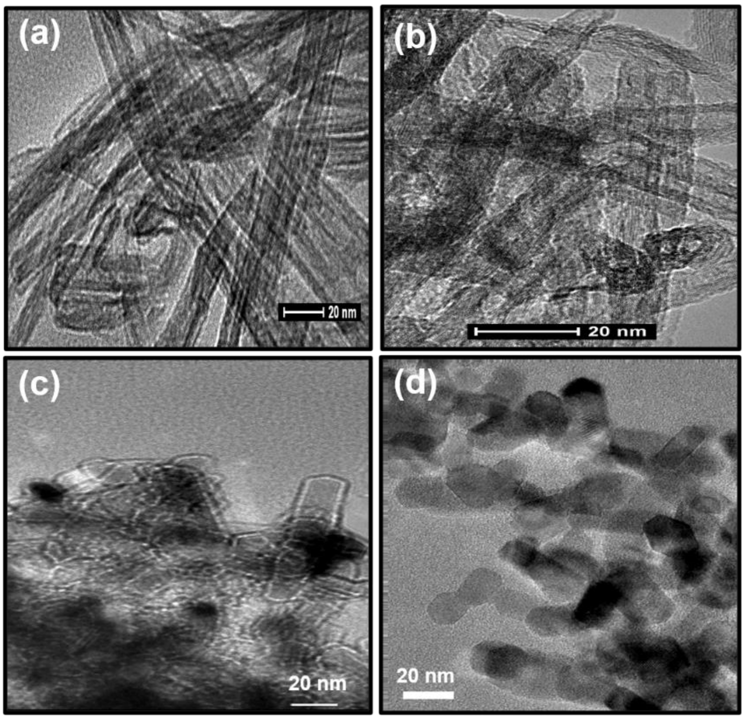

Figure 4: TEM micrographs of (a) HT150, (b) HT150/400, (c) HT150/500, and (d) HT150/700

Table 1 summarizes the Brunauer-Emmett-Teller (BET) surface areas of the HT150, HT150/400, HT150/500, and HT150/700 samples. The pristine HT150 sample exhibited the highest surface area, at 252.66 m²/g. This value decreased slightly to 224.80 m²/g for HT150/400. This reduction can likely be attributed to the limited accessibility of N_2 gas to the tightly packed structure formed by the aggregation of nanotubes during calcination at 400 °C. A more significant decrease in surface area was observed for the HT150/500 sample (114.22 m²/g), likely due to the substantial destruction of the tubular structure and its transformation into nanoparticles [15]. The HT150/700 sample possessed the lowest surface area (35.33 m²/g), attributable to particle coarsening and pore coalescence at the higher calcination temperature, resulting in a significantly lower surface area compared to the other samples. The pore volume of the samples also displayed a decreasing trend, ranging from 1.22 cm³/g to 0.46 cm³/g. Notably, the pore size distribution analysis revealed that all samples possess mesopores, with pore diameters between 30 and 10 nm.

Table 1: Surface area, pore size and pore volume of HT150, HT150/400, HT150/500, and HT150/700

Samples	**Surface area (m^2/g)**	**Pore volume size (cm^3/g)**	**Pore size (nm)**
HT150	264.26	1.22	18.64
HT150/400	224.80	1.02	26.82
HT150/500	114.22	0.98	25.41
HT150/700	35.31	0.46	12.82

Fig. 5 presents the photocatalytic performance of HT150, HT150/400, HT150/500, and HT150/700 samples for methyl orange (MO) degradation. The pristine HT150 sample exhibited the lowest activity, degrading only 13.38% and 34.88% of MO after 180 minutes of reaction. This can be attributed to its titanate structure, as confirmed by XRD and Raman analysis. Titanate structures are generally considered less suitable for photocatalysis due to their highly crystalline nature, hindering efficient charge separation and electron transfer [16,17]. The titanate compounds exhibit an increased abundance of Ti-O bonds, particularly in hydrogen titanates. This excess oxygen within the layered nanotubes can impede the transfer of interfacial charges and hinder the efficient acceptance of photogenerated electrons [18]. This limitation likely explains the low photocatalytic activity observed for the titanate nanotube structure in HT150, with MO removal potentially occurring solely through adsorption onto the nanotubes. In contrast, the HT150/400 sample displayed the highest MO degradation (80.12%) after 3 hours of UV irradiation. This superior performance can be attributed to the presence of anatase phase TiO_2 with a tubular morphology. The tubular morphology promotes the diffusion of reactants and products, enhancing photocatalytic activity by facilitating access to active sites on the catalyst surface [19]. Additionally, this structure can accelerate the mass transfer of adsorbed molecules from the bulk solution to the catalyst surface, further promoting the photocatalytic process [20]. However, the photocatalytic activity of the HT150/500 sample shows a slight decrease compared to HT150/400. This is likely due to thermal damage to the nanotubes and the transformation of the surface morphology into irregular particles during calcination at a high temperature [21]. The performance of the HT150/700 sample for MO degradation is further reduced due to the agglomeration of these irregular particles, which presumably reduces the surface area and consequently, the photocatalytic activity of the material.

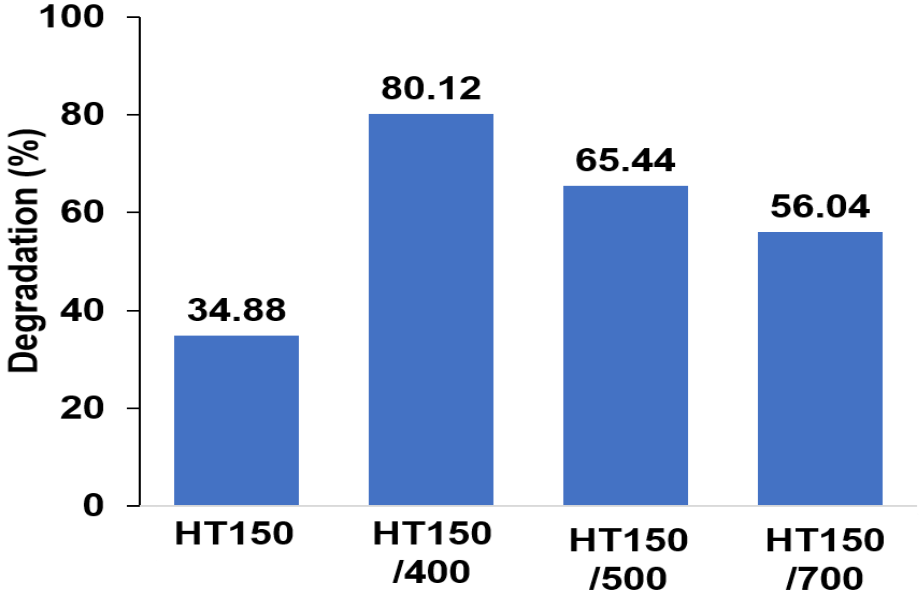

Figure 5: Photocatalytic degradation of MO in the presence of HT150, HT150/400, HT150/500, and HT150/700 samples for methyl orange (MO) degradation.

Antibacterial activity of HT150/400 against *Staphylococcus aureus (S. aureus)* bacteria strains was carried out using disc diffusion method. These bacteria were used because they can caused severe infection on the skin and other soft tissues of the body [22]. Positive antibacterial result was indicated by the occurrence of clear inhibition zones around the discs and their activity was determined by measuring the diameter of clear zone of inhibition. The measured inhibition zone were 8.06±0.08 mm, 10.12±0.18 mm, 12.44±0.25 mm, 14.01±0.22 mm, and 15.44±0.26 mm against *S. aureus*, for HT150/400 sample of 0.01, 0.05, 0.01, 0.015 and 0.2 M, respectively. The result obtained suggesting that, HT150/400 nanostructures is a promising antibacterial agent. Good antibacterial activity by HT150/400, suggested due to formation of TiO_2 nanotube’s structure. It is suggested that when TiO_2 comes into contact with a microorganism, photo-generated reactive oxygen species (ROS) can enter the cell through a diffusion process that causes oxidative damage of cellular molecules, such as carbohydrates, lipids, proteins and nucleic acids, leading to cell death [23]. In addition, ROS can disrupt the cell wall through lipid peroxidation and thus interrupt the transmembrane electron transport [24]. If TiO_2 particles are small in size, they can penetrate the cell and photo-generation of ROS can occur inside the cell [25-27]. The HT150/400 at highest concentration (0.20 M) displays the highest exhibition zone due to generation of more ROS.

Conclusion

This study successfully demonstrated the transformation of hydrogen titanate nanotubes (HT150) into various TiO_2 nanostructures with tunable photocatalytic and antibacterial properties. By methodically altering the calcination temperature, the researchers were able to control the resulting TiO_2 phase and morphology, producing distinct nanostructures such as nanotubes, nanoparticles, and irregularly shaped particles. The ability to adjust these parameters is critical, as it directly influences the material's functional properties. Calcination temperature was identified as a crucial factor in determining the TiO_2 phase and morphology. For instance, at specific temperature ranges, the transformation led to the formation of the anatase phase, which is known for its superior photocatalytic properties. The study showed that TiO_2 with a tubular morphology, resulting from a controlled calcination process, demonstrated exceptional photocatalytic activity, achieving over 80% degradation of methyl orange, a common dye used in environmental testing. This significant photocatalytic performance underscores the importance of precise control over both the phase and morphology of the TiO_2 nanostructures to optimize their functional capabilities. The anatase phase TiO_2 with tubular morphology exhibited superior photocatalytic activity for methyl orange degradation compared to other structures. The tubular form offers a high surface area, which is advantageous for catalytic reactions, as it provides more active sites for the interaction with pollutants. The higher photocatalytic activity is likely due to the unique electronic properties of the anatase phase, which facilitates efficient charge separation and reduces electron-hole recombination, a common issue that can decrease photocatalytic efficiency. This highlights the importance of morphology and phase control for optimizing photocatalytic performance, suggesting that specific structural characteristics can significantly enhance the material's ability to degrade organic contaminants. The study also explored the antibacterial efficacy of the synthesized TiO_2 nanostructures. It was found that the antibacterial properties varied depending on the concentration of the nanostructures used. The research demonstrated that TiO_2 nanotubes could achieve a significant inhibition zone against *Staphylococcus aureus*, a common and potentially harmful bacterium. The recorded inhibition zone measured 15.44±0.26 mm, indicating a substantial antibacterial effect. This finding suggests that by controlling the structure and concentration of the TiO_2 nanostructures, it is possible to tailor these materials for specific antibacterial applications. The tubular morphology may provide a larger contact area with bacterial cells, enhancing the material's ability to disrupt bacterial membranes or generate reactive oxygen species that can kill bacteria. Overall, this work presents hydrogen titanate nanotubes as a promising precursor material for the development of efficient photocatalysts and antibacterial agents. The ability to transform these nanotubes into various TiO_2 nanostructures through controlled calcination processes allows for the fine-tuning of their properties to meet specific application requirements. By manipulating the calcination process, desired functionalities such as enhanced photocatalytic activity or targeted antibacterial action can be achieved. This capability opens doors to the design of novel and versatile materials for environmental remediation, such as water and air purification, and disinfection applications, including antibacterial coatings and surfaces. The study highlights the potential for further research into the optimization of these materials to address a wide range of environmental and health-related challenges.

Acknowledgements

The authors are grateful to Universiti Malaysia Terengganu (UMT) for facilities and Malaysia Ministry of Higher Education for the financial support vote (FRGS/1/2023/STG05/UMT/02/7).

References

1. Zhao, J.W., Wang, H.Y., Feng, L., Zhu, J.Z., Liu, J.X. and Li, W.X., 2023. Crystal-Phase Engineering in Heterogeneous Catalysis. *Chemical Reviews*, *124*(1), pp.164-209.
2. Kusior, A., Jeleń, P., Sitarz, M., Świerczek, K. and Radecka, M., 2023. 3D Flower-like TiO2 Nanostructures: Anatase-To-Rutile Phase Transformation and Photoelectrochemical Application. *Catalysts*, *13*(4), p.671.

3. Gu, Q., Long, J., Zhou, Y., Yuan, R., Lin, H. and Wang, X., 2012. Single-site tin-grafted anatase TiO2 for photocatalytic hydrogen production: Toward understanding the nature of interfacial molecular junctions formed in semiconducting composite photocatalysts. *Journal of catalysis*, *289*, pp.88-99.
4. Rui, Z., Wu, S., Peng, C. and Ji, H., 2014. Comparison of TiO2 Degussa P25 with anatase and rutile crystalline phases for methane combustion. *Chemical Engineering Journal*, *243*, pp.254-264.
5. Wu, S., 2021. Flame synthesis of nanostructured TiO2 for energy and environmental applications.
6. Reghunath, S., Pinheiro, D. and KR, S.D., 2021. A review of hierarchical nanostructures of TiO2: Advances and applications. *Applied Surface Science Advances*, *3*, p.100063.
7. Liu, Y., Wang, Z., Wang, W. and Huang, W., 2014. Engineering highly active TiO2 photocatalysts via the surface-phase junction strategy employing a titanate nanotube precursor. *Journal of catalysis*, *310*, pp.16-23.
8. Liu, G., Yang, H.G., Pan, J., Yang, Y.Q., Lu, G.Q. and Cheng, H.M., 2014. Titanium dioxide crystals with tailored facets. *Chemical reviews*, *114*(19), pp.9559-9612.
9. Meenakshi, P. and Selvaraj, M., 2018. Bismuth titanate as an infrared reflective pigment for cool roof coating. *Solar Energy Materials and Solar Cells*, *174*, pp.530-537.
10. Li, N., Yuan, M., Xu, J., Li, X., Wang, G., Zhu, X. and Li, C., 2024. Efficient synthesis of the di-tert-butyl peroxide by isobutane selective peroxidation with molecular oxygen over sulfated titanium oxide. *Molecular Catalysis*, *553*, p.113770.
11. Kassem, L.M., Zaki, A.H., El-Deen, A.G. and El-Dek, S.I., 2024. Synthesis of Titanate Nanotube for Antibacterial and Tissue Regeneration Applications. *Inorganic Chemistry Communications*, *161*, p.112038.
12. Yun, S.Y., Lee, S., Jin, X., Soon, A. and Hwang, S.J., 2024. Ammonolysis-Driven Exsolution of Ru Nanoparticle Embedded in Conductive Metal Nitride Matrix to Boost Electrocatalyst Activity. *Advanced Science*, p.2309819.
13. Duran-Toscano, A.A., de León-Hernández, J.D., Fuentes-Moyado, S., Medina-Martínez, J.A., Hernández-Torres, J., García-González, L., Martínez-Castillo, J., Guzmán-Navarro, G., Domínguez-Nicolás, S.M. and Hernández-Quiroz, T., 2024. Synthesis and characterization of Fe3O4 core nanoparticles coated with TiO2 and ZnO. *Nano-Structures & Nano-Objects*, *38*, p.101138.
14. Saravanan, S., Dubey, R.S. and Subbarao, P.S., 2023. Optical investigation of sol–gel-synthesized and spin-coated SiO2/TiO2 multilayers. *Nanomaterials and Energy*, *12*(1), pp.44-48.
15. Rachmaniar, S., Nugraha, D.A., Santjojo, D.J., Tjahjanto, R.T., Mufti, N. and Masruroh, 2024. Prevention of particle agglomeration in sol–gel synthesis of TiO2 nanoparticles via addition of surfactant. *Journal of Nanoparticle Research*, *26*(3), p.45.
16. Wang, Q., Yang, X., Jing, Z., Liu, H., Tang, P., Zhu, H. and Li, B., 2024. Recent advances in one-dimensional alkali-metal hexatitanate photocatalysts towards environmental remediation and solar fuel production. *Journal of Materials Science & Technology*.
17. Pereira, C.A., Amoresi, R.A., Teixeira, G.F., Oliveira, R.C., Coleto Jr, U., da Luz, A.R., de Almeida, P.B., Simões, A.Z., Monteiro Filho, E.S., Longo, E. and Perazolli, L.A., 2023. Effect of chemical potential on the structural modification of titanate-based photocatalysts: Fast dye degradation efficiency and adsorption power. *Journal of Alloys and Compounds*, *947*, p.169691.

18. Gonzalez, V. R., Alfaro, S. O., Lozano-Sáncheza, L. M., Soo-Wohn L. (2012). Rapid microwave-assisted synthesis of one-dimensional silver–$H_2Ti_3O_7$ nanotubes. *Journal of Molecular Catalysis A: Chemical*, 353– 354 (2012), pp. 163 – 170.
19. Huang, K.C. and Chien, S.H., 2013. Improved visible-light-driven photocatalytic activity of rutile/titania-nanotube composites prepared by microwave-assisted hydrothermal process. *Applied Catalysis B: Environmental*, *140*, pp.283-288.
20. Huo, S., Zhao, Q., Fu, W., Wu, X., Wang, Y., Haijiao, X. and Gao, M., 2024. Porous MnxFe3-xO4 spinel oxides trigger H2O2 activation for boosted degradation of tetracycline: The formation and dominant role of surface-bound radicals. *Separation and Purification Technology*, p.127555.
21. Fu, N., Chen, H., Chen, R., Ding, S. and Ren, X., 2023. Effect of Calcination Temperature on the Structure, Crystallinity, and Photocatalytic Activity of Core-Shell SiO2@ TiO2 and Mesoporous Hollow TiO2 Composites. *Coatings*, *13*(5), p.852.
22. Ahmed, J., Arfat, Y.A., Castro-Aguirre, E. and Auras, R., 2016. Mechanical, structural and thermal properties of Ag–Cu and ZnO reinforced polylactide nanocomposite films. *International journal of biological macromolecules*, *86*, pp.885-892.
23. Rashid, M.M., Simončič, B. and Tomšič, B., 2021. Recent advances in TiO2-functionalized textile surfaces. *Surfaces and Interfaces*, *22*, p.100890.
24. Xiang, Z., Xu, Y., Dong, W., Zhao, Y. and Chen, X., 2024. Effects of sliver nanoparticles on nitrogen removal by the heterotrophic nitrification-aerobic denitrification bacteria Zobellella sp. B307 and their toxicity mechanisms. *Marine Pollution Bulletin*, *203*, p.116381.
25. Hajipour, M.J., Fromm, K.M., Ashkarran, A.A., de Aberasturi, D.J., de Larramendi, I.R., Rojo, T., Serpooshan, V., Parak, W.J. and Mahmoudi, M., 2012. Antibacterial properties of nanoparticles. *Trends in biotechnology*, *30*(10), pp.499-511.
26. Regmi, C., Joshi, B., Ray, S.K., Gyawali, G. and Pandey, R.P., 2018. Understanding mechanism of photocatalytic microbial decontamination of environmental wastewater. *Frontiers in chemistry*, *6*, p.33.
27. Díez-Pascual, A.M., 2018. Antimicrobial coatings based on linseed oil/TiO2 nanocomposites. *Handbook of Antimicrobial Coatings*, p.411.